RSC Advances

PAPER

View Article Online
View Journal | View Issue

Cite this: *RSC Adv.*, 2026, **16**, 5252

Adsorption of methylisocyanate and ethylisocyanate on a Co-decorated TiS_2 monolayer: understanding chemical interactions using DFT and COHP

Raja Naveed Ahmed,[a] Zhang Leilei,[b] Muhammad Abdul Rauf Khan,[a] Iltaf Muhammad,[c] Azhar Ahmed,[a] Zulfiqar Ali,[d] Alishba Zareen[a] and Muhammad Mushtaq *[a]

Designing efficient nanosensors is highly desirable for the detection of toxic substances. Herein, the adsorption behavior of the two specified VOCs, methylisocyanate (MIC) and ethylisocyanate (EIC), was investigated using density functional theory (DFT) and COHP calculations on pristine and cobalt-decorated titanium disulfide (Co–TiS_2) monolayer systems. The decoration of Co on the TiS_2 monolayer induces a semiconductor-to-metal transition in it. The stability of the Co–TiS_2 monolayer system was confirmed by the calculated adsorption energy (E_{ads}) of −3.18 eV. DFT calculations revealed that the pristine TiS_2 monolayer systems are chemically inert towards the above-specified VOCs. However, functionalizing the TiS_2 monolayer with a Co atom substantially improved the adsorption of MIC and EIC molecules. The estimated E_{ads} values upon MIC and EIC adsorption on Co–TiS_2 monolayer systems were −0.81 eV and −0.95 eV, respectively. The adsorption of the investigated VOCs changed the electronic and magnetic properties of Co–TiS_2 monolayer systems, which were examined through spin-polarized density of states calculations. Bader charge analysis revealed that VOCs are charge acceptors and the Co–TiS_2 monolayer is a charge donor. A considerable increase in work function was observed upon adsorption, correlating with sensitivity enhancements of up to 10% for MIC and 8% for EIC. COHP analysis revealed that both molecules interact with the adsorbent by forming Co–N ionic bonding caused by the Co(4s)-N(2s) orbital overlapping. The Ti–S, Co–S, and Co–N bonding pairs possess an ICOBI value of 0.32, 0.31, and 0.15, respectively, showing weak ionic bonding. Our findings propose that Co–TiS_2 could be a better choice for the detection of MIC and EIC.

Received 28th November 2025
Accepted 17th January 2026

DOI: 10.1039/d5ra09215a

rsc.li/rsc-advances

1 Introduction

The uncontrolled release of toxic gases and volatile organic compounds (VOCs) from industrial activities, automobile exhaust, and the routine usage of organic solvents in paints, adhesives, and other products into the environment is deteriorating living standards and food safety.[1,2] VOCs belonging to the family of low-molecular-weight compounds, consist of carbon and hydrogen atoms, and vaporize easily at ambient conditions.[3] The dermal contact or inhalation of VOCs has both acute and chronic impacts on human health.[4] Short-term exposure to VOCs can lead to eye and throat irritation, headaches, and dizziness.[5,6] In contrast, long-term exposure has been associated with skin allergies, hormonal imbalances, neurotoxicity, cancer, kidney damage, and effects on reproductive and metabolic functions.[7–9]

Methyl isocyanate (MIC), a member of the VOCs family, with the chemical formula C_2H_3NO, is a colorless, highly flammable liquid having a sharp, strong smell.[10] It rapidly evaporates when exposed to air. MIC is extensively used in the synthesis of polyurethane foams, plastics, rubbers, and adhesives, as well as in the production of carbamate pesticides.[11] Even though it is useful, but has a reactive and highly toxic nature, creating several health hazards, including reproductive and developmental toxicity, respiratory irritation, cancer, and even death.[12,13] The deaths of about 8000 people within 48 hours were reported due to the leakage of MIC in the Bhopal disaster, leaving more than 200 000 victims who were experiencing long-term health consequences.[14] Ethyl isocyanate (EIC), a derivative of the isocyanate family, is a colorless, transparent, flammable liquid with a pungent smell. The electrophilic nature of the

[a]*Department of Physics, University of Poonch Rawalakot, Rawalakot 12350, Pakistan. E-mail: mushtaq325@gmail.com*

[b]*Henan Key Laboratory of Nanocomposites and Applications, Institute of Nanostructured Functional Materials, Huanghe Science and Technology College, Zhengzhou, Henan 450006, PR China*

[c]*School of Mechanical and Electrical Engineering, Hainan Vocational University of Science and Technology, Haikou 571126, China*

[d]*School of Physics and Optoelectronic Engineering, Beijing University of Technology, Beijing, 100124, China*

isocyanate unit in its structure makes it suitable for the synthesis of various organic compounds. Although it is used as an intermediate for the synthesis of agrochemicals, pharmaceuticals, and polyurethane-based materials, it has some adverse health effects.[15] Its acute exposure can induce irritation in the eyes and cause skin allergies, while chronic exposure may lead to shortness of breath, wheezing, cough, and chest infections.[16] Considering the challenges of health and safety in the laboratory and industry, the detection of VOCs, such as MIC and EIC, is inevitable.

Metal oxide-based nanosensors have mainly been used for the detection of VOCs because of their excellent sensing potential and ease of operation. Still, high operating temperature and poor sensitivity have limited their feasibility for sensing purposes.[17,18] Sensors based on conducting polymers are also not suitable for detecting VOCs due to certain drawbacks, such as degradation and humidity effects.[19] Two-dimensional (2D) materials have attracted considerable attention in sensor technology owing to their large surface-to-volume ratio and high density of active sites.[20] Among 2D materials, thanks to their tunable band gap and sensitive surfaces, transition metal dichalcogenides (TMDs) have received considerable attention for sensor applications.[21] Within the family of TMDs, the titanium disulfide (TiS_2) remains unexplored for VOCs sensing applications. TiS_2 is a layered TMD similar to MoS_2 and WS_2; however, its crystallographic structure differs significantly, crystallizing in a CdI_2-type hexagonal close-packed (hcp) phase.[22] A monolayer TiS_2 nanosheet is composed of a layer of Ti atoms positioned between two S atomic layers. TiS_2 can crystallize in different polymorphs, most notably the 1T and 2H phases. In the 1T phase, each Ti atom is coordinated by six S atoms in an octahedral coordination environment. Whereas, in the 2H phase, Ti atoms are surrounded by six S atoms arranged in a trigonal prismatic geometry.[23] TiS_2 favors the 1T phase over the 2H phase, being 142 meV per atom lower in energy.[24] Henceforth, the analysis pertains to the 1T phase. The weak interlayer bonding in TiS_2 enables the isolation of individual monolayers. Several techniques, such as atomic layer deposition, chemical vapor deposition, and exfoliation techniques, have been employed for the synthesis of 2D TiS_2.[25,26]

The sensing efficiency of a pristine TMDs monolayer sensor towards adsorbates is relatively weak, but can be enhanced through various approaches, like heterojunction engineering, doping, exposure to high-energy beams, morphology modification, and decoration with metals.[27–31] H. Liu *et al.* reported using first-principles calculations that the Ir-decorated MoS_2 exhibits good potential for detecting C_2H_2 and C_2H_4 gas molecules.[32] H. Wu *et al.* showed that Pd decoration improves the H_2 sensing behavior of MoS_2.[33] J. Shi *et al.* reported that doping TaS_2 with metal atoms not only tunes the Fermi level but also introduces positive charge centers, which contribute to superior gas-sensing performance.[34] F. Altalbawy *et al.* performed the DFT simulation to examine the Pd and Pt transition metals decorated WS_2 nanosheets for the efficient detection of SO_2 and SO_3 molecules.[35] Toularoud *et al.* studied the electronic and magnetic properties of monolayer TiS_2 doped with 3d transition-metal atoms and found that the Cr-doped TiS_2 monolayer system showed the most significant magnetic moment.[36] Ghani *et al.* emphasized that the presence of defects in TiS_2 monolayers enhances their adsorption of CO molecules.[37] T. Tang *et al.* reported that titanium oxysulfide (TiS_xO_{2-x}) significantly improves the sensitivity and stability of NO_2 detection at room temperature.[38] S Zhang *et al.* have made a COHP analysis of metal-doped WSe_2 to analyze the bonding and antibonding interactions between the adsorption sites and gas molecules.[39] To the best of our knowledge, transition-metal-decorated TiS_2 has not yet been investigated for the efficient detection of VOCs like MIC and EIC. Therefore, it is of great interest to analyze the adsorption behavior and sensing mechanisms governing the interaction of targeted VOCs on the surface of 2D TiS_2. Hence, analyzing how VOCs adsorb and interact with TiS_2 monolayer systems is essential for understanding their sensing performance.

This study examines the structural, electronic, and magnetic properties of pristine TiS_2 (p-TiS_2) and cobalt-decorated TiS_2 (Co–TiS_2) monolayers for the adsorption of MIC and EIC using DFT calculations. To characterize the adsorption mechanism, we consider adsorption energy, adsorption height, charge transfer, and the modifications in electronic and magnetic properties. Additionally, electron localization function (ELF) and crystal orbital Hamiltonian population (COHP) analysis was employed to illustrate the bonding interactions between Co–TiS_2 monolayer systems and the adsorbed VOCs molecules. Thus, this study offers a theoretical foundation for developing efficient VOCs sensors.

2 Computational method

In the present study, first-principles calculations were performed with the Vienna *Ab initio* Simulation Package (VASP) code based on density functional theory (DFT).[40] The projector-augmented wave (PAW) potentials were considered to describe the interactions between the electron and ions.[41] For treating electron interactions, the exchange-correlation energy was described using the generalized gradient approximation (GGA) within the Perdew–Burke–Ernzerhof (PBE) functional.[42] To consider the long-range interactions, van der Waals (vdW) effects were incorporated using the Grimme correction (*i.e.*, DFT-D3) with a vdW correction parameter (IVDW) of 12.[43] The on-site coulomb interactions between partially filled d-orbitals of Ti and Co atoms were corrected using the DFT + U_{eff} approach, where U_{eff} for Co and Ti are 3.42 eV and 2.58 eV, respectively.[44] A cutoff kinetic energy of 500 eV was employed for the plane-wave expansion, and the size of the *k*-point mesh was set to 25 × 25 × 1, which was validated through convergence tests and presented in Fig. S11. For initial calculations, a unit cell of the pristine T-TiS_2 monolayer was obtained from the TiS_2 bulk structure, and a 20 Å vacuum along the *z*-axis was used to avoid interactions between periodic images. The convergence criterion of 10^{-5} eV and smearing width of 0.0 eV was used for full relaxation of the 1 × 1-TiS_2 unit cell. To investigate the effect of Co-decoration, a supercell of 5 × 5 × 1 was constructed from a 1 × 1 TiS_2 unit cell, and the *k*-point mesh of 4 × 4 × 1 was employed for its geometry optimization. To analyze the

stability of the Co-decorated TiS_2 monolayer systems and the adsorbed molecules, the following equation was used.[45]

$$E_{ads} = E_{Co-TiS_2} - E_{TiS_2} - E_{Co} \quad (1)$$

where E_{Co-TiS_2} denotes the total energy of the Co–TiS_2 monolayer systems E_{TiS_2} refers to the total energy of TiS_2 monolayer systems, and E_{Co} corresponds to that of the isolated Co-atom.

The adsorption energies (E_{ads}) of the selected VOCs on Co–TiS_2 monolayer systems were calculated using the expression.

$$E_{ads} = E_{VOC/Co-TiS_2} - E_{Co-TiS_2} - E_{VOC} \quad (2)$$

where $E_{VOC/Co-TiS_2}$ denotes the total energy of the VOCs adsorbed Co–TiS_2 monolayer systems E_{Co-TiS_2} refers to the total energy of Co–TiS_2 monolayer systems, and E_{VOC} Corresponds to that of the isolated VOC molecule.

The equation used for the calculation of work function (Φ) was.[46]

$$\phi = E_{vacuum} - E_F \quad (3)$$

where E_F is the Fermi energy and E_{vacuum} is the vacuum-level electrostatic potential energy.

The charge density difference (CDD) was calculated by using the equation.[47]

$$\Delta\rho = \rho_{product} - \rho_{adsorbent} - \rho_{molecule} \quad (4)$$

where $\rho_{product}$, $\rho_{adsorbent}$ and $\rho_{molecule}$ are the total charge density of the VOCs adsorbed Co–TiS_2 monolayer systems, bare Co–TiS_2 surface, and isolated VOCs, respectively.

3 Results and discussions

3.1 Structural properties of p-TiS_2 and Co–TiS_2

Our discussion starts with the structural properties of p-TiS_2 and Co–TiS_2 monolayer systems. To find the ground state energy of p-TiS_2, it was subjected to full structural relaxation for both non-magnetic and magnetic configurations. The results confirm that p-TiS_2 is non-magnetic, as reported in the literature.[48] For the decoration of TiS_2 with Co, five different possible adsorption sites were considered, namely the bridge site, hollow site, lower S site, Ti top site, and upper S site, as shown in Fig. S1. The bridge site corresponds to the midpoint of the Ti–S bond, the hollow site lies above the center of the hexagonal ring, the lower S site is positioned above the S atom in the bottom layer, the Ti top site is directly above a Ti atom, and the upper S site is located above the S atom in the top plane of the TiS_2 monolayer. Each configuration was subjected to full relaxation for various magnetic and non-magnetic states. Based on the computed ground-state energies and from the estimated adsorption energy (E_{ads}), Co adsorption at the hollow site is found to be most energetically favorable. Xu *et al.* examined Sc adsorption on WS_2 and found that the hexagonal hollow site offered the most energetically favorable configuration.[49] Furthermore, the lowest energy is achieved in the ferromagnetic (FM) configuration, verifying that Co–TiS_2 favors a ferromagnetic (FM) ground state, in agreement with earlier studies.[50]

The optimized geometry of p-TiS_2 is presented in Fig. 1(a). TiS_2 crystallizes in a hexagonal lattice structure, and side-view analysis reveals a tri-layer structure, with the Ti layer centrally positioned between two symmetric S layers. The ground state lattice constant of p-TiS_2 monolayer is $a = b = 3.42$ Å, and the Ti–S bond length is 2.42 Å, whereas in the literature, the reported values are 3.40 Å and 2.42 Å, respectively.[51] The observed S–Ti–S bond angles are 90.66° and 54.80°. The vertical distance separating the upper and lower sulfur atom planes in monolayer TiS_2 is known as the buckling height or thickness of the monolayer, and its observed value is 2.84 Å. The optimized top and side views of the five distinct Co–TiS_2 configurations are illustrated in Fig. S2. This demonstrates that in each case, the Co atom undergoes a slight displacement from its initial position to achieve a more stable configuration. The ground state lattice constant of the Co–TiS_2 monolayer is observed to be $a = b = 3.42$ Å, identical to that of pristine TiS_2, while the Ti–S bond length slightly increases to 2.43 Å upon decoration. The change in bond length may be attributed to the interaction between the Co atom and the substrate.[52] The adsorption energy for each configuration is calculated and is presented in Table 1. The negative E_{ads} indicated that the decoration of the Co atom on the surface of the TiS_2 is an exothermic process.[53] Moreover, to verify the thermal stability of Co–TiS_2, *ab initio* molecular dynamics (AIMD) simulations were performed at 300 K for 6000 fs and presented in Fig. S12. It is observed that despite some minor distortions, the structure did not dissociate into an amorphous phase. No local bond breaking is observed. The potential energy PE of the ions has some clear fluctuations at some intervals. These peaks correspond to the large displacement of the Co atom from the initial position. However, as the simulation process evolves, the PE variation becomes smaller. It shows the local geometry does not undergo large changes or distortions. The displacement of the Co atom also has some

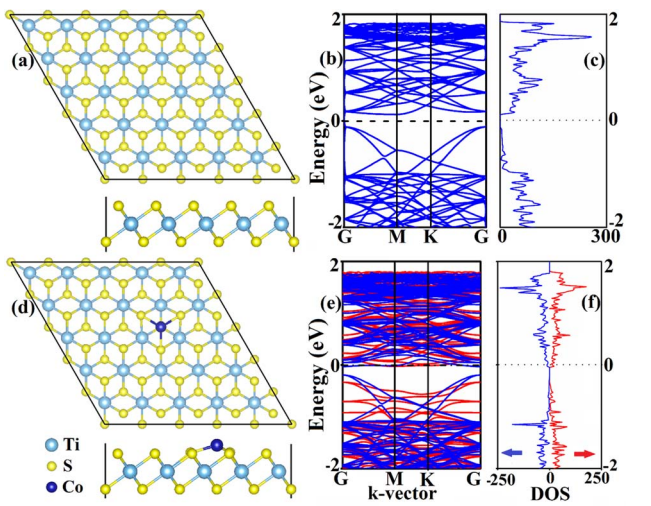

Fig. 1 (a and d) Optimized structures, (b and e) band structures, and (c and f) the total density of states (TDOS) of p-TiS_2 and Co–TiS_2 monolayers, respectively.

Table 1 A summary of adsorption energy (E_{ads}) in eV of Co-atom decorated TiS_2 monolayer at different adsorption sites, magnetic moment in μ_B, vertical distance (h) between Co-atom and upper S-atom layer in Å, Co–S bond length in Å, and nature of adsorption for each configuration

System	Adsorption configuration	Magnetic moment	E_{ads}	h	Co–S bond length	Adsorption
Co-decorated TiS_2	Bridge site	−2.52	−3.07	1.10	2.27	Chemisorption
	Hollow site	−2.65	−3.18	0.66	2.16	Chemisorption
	Lower S site	−2.65	−2.98	0.71	2.17	Chemisorption
	Ti top site	−2.52	−3.13	1.10	2.26	Chemisorption
	Upper S site	−2.80	−1.48	2.19	2.15	Chemisorption

variations; however, these can be regarded as small. It shows that the given structure is assumed to be thermally stable.

3.2 Electronic and magnetic properties of p-TiS_2 and Co–TiS_2

To understand how Co decoration modifies the electronic and magnetic behavior of the TiS_2 monolayer, we performed a detailed analysis of its electronic band structure and density of states (DOS), providing deeper insights into the underlying mechanisms of property modulation. The calculated electronic band structure and total density of states (TDOS) of the p-TiS_2 monolayer system are shown in Fig. 1(b and c). From Fig. 1(b), the missing electronic states at the Fermi level indicate that p-TiS_2 is a semiconductor. The valence band maximum (VBM) lies at the G point, whereas the conduction band minimum (CBM) appears at the M point. Thus, the material exhibits an indirect band gap nature. The CBM is positioned 0.11 eV above the Fermi level, while the VBM lies 0.11 eV below it, yielding a band gap of 0.22 eV, which closely matches the previously reported value of 0.18 eV.[54] The density of states (DOS) analysis, as presented in Fig. 1(c), further confirms the presence of an energy gap in the p-TiS_2 monolayer system due to the absence of states around the Fermi level. To gain deeper insights into the electronic properties, the partial density of states (PDOS) and orbital density of states (ODOS) of the p-TiS_2 monolayer were examined and are presented in Fig. 2(a–c). From the PDOS analysis, it is evident that both Ti and S atoms contribute to the electronic states around the band edges. The VBM is primarily derived from the 3p orbitals of S atoms, while the 3d orbitals of Ti atoms dominate the CBM. The spin-polarized electronic band structure and TDOS of the Co–TiS_2 monolayer system are presented in Fig. 1(e and f), respectively. The decoration of Co on the TiS_2 monolayer induces a semiconductor-to-metal transition in it, as seen by the presence of electronic states at the Fermi level in Fig. 1(e). This behavior is consistent with the findings of U. Iqrar *et al.*, who observed a similar transition upon the decoration of Li, Na, and K on TiS_2.[55] Decoration with a foreign atom may distort the host lattice charge distribution, introducing new states near the Fermi level that increase the density of states and facilitate electron occupation, thereby enhancing conductivity.[56] The TDOS, PDOS, and ODOS spectra of Co–TiS_2 are presented in Fig. 2 (d–f). The Ti-3d orbitals contribute to the conduction band, while the Co-3d and S-3p orbitals dominate the valence band. The spin-polarized TDOS plot of Co–TiS_2 from Fig. 1(f) shows an unequal distribution of density of states between spin-up and spin-down channels, leading to a net magnetization in the Co–TiS_2 monolayer system.[57] The estimated total magnetic moment is −2.65 μ_B, where the negative sign indicates that the majority of carriers occupy the spin-down channel, also depicted in plot 1(f). The Co contributes to this magnetic moment is −1.902 μ_B, whereas Ti-atoms contribute −0.055 μ_B. The negative signs indicate that the Co atom and the Ti atoms are spin-polarized in parallel, and the Co–TiS_2 monolayer system is ferromagnetic. Upon Co decoration, the partially filled 3d orbitals of Co introduce unpaired electrons and spin polarization, thereby inducing magnetism in the system. Whereas in p-TiS_2, Ti^{4+} cations possess an empty 3d shell and therefore do not contribute any unpaired d electron to the system, and the system remains non-magnetic.

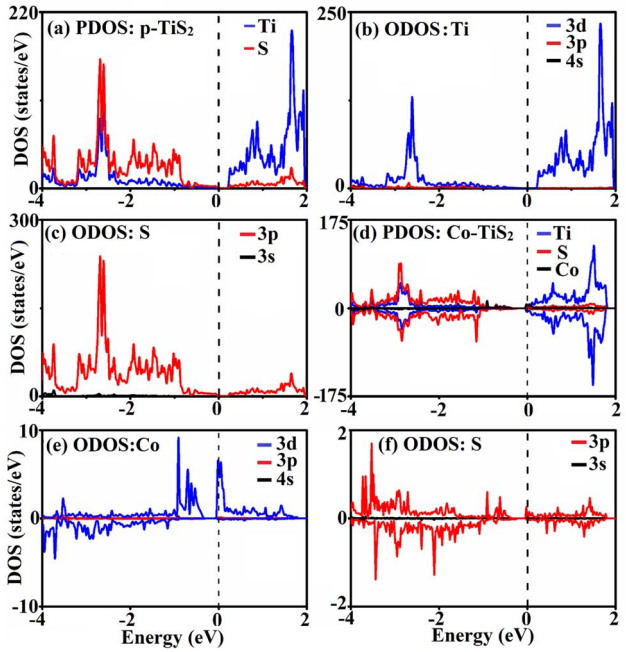

Fig. 2 Partial density of states (PDOS) and orbital density of states (ODOS); (a–c) for p-TiS_2 and (d–f) for Co–TiS_2.

4 Adsorption of MIC and EIC molecules

To explore the adsorption behavior of MIC and EIC on TiS_2 monolayer systems, six different possible initial orientations of the adsorbates, four parallel (h_1, h_2, h_3, and h_4) and two perpendicular (v_1 and v_2) to the surface, were considered, and

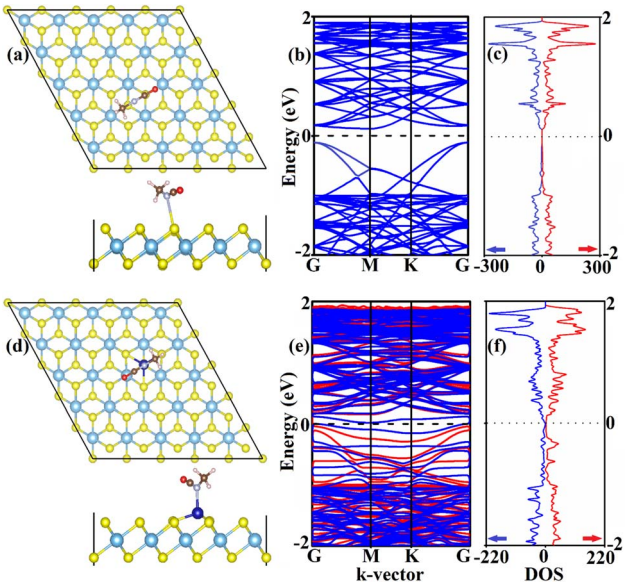

Fig. 3 (a and d) Optimized structures, (b and e) band structures, and (c and f) TDOS of methylisocyanate (MIC) adsorbed on p-TiS_2 and Co–TiS_2 surfaces, respectively.

the corresponding ground state energies were calculated. All the initial configurations are shown in Fig. S3 and S5. The relaxed geometries corresponding to the most stable orientations of MIC and EIC on p-TiS_2 are presented in Fig. 3(a) and 4(a), respectively. Our calculations revealed that both MIC and EIC preferentially adsorb on p-TiS_2 *via* the O site, forming a Co–O bond perpendicular to the plane. The key parameters characterizing the optimized adsorption configurations are given in Table 2. The calculated E_{ads} of MIC and EIC on p-TiS_2 monolayer are −0.15 eV and −0.17 eV, respectively. The optimized average

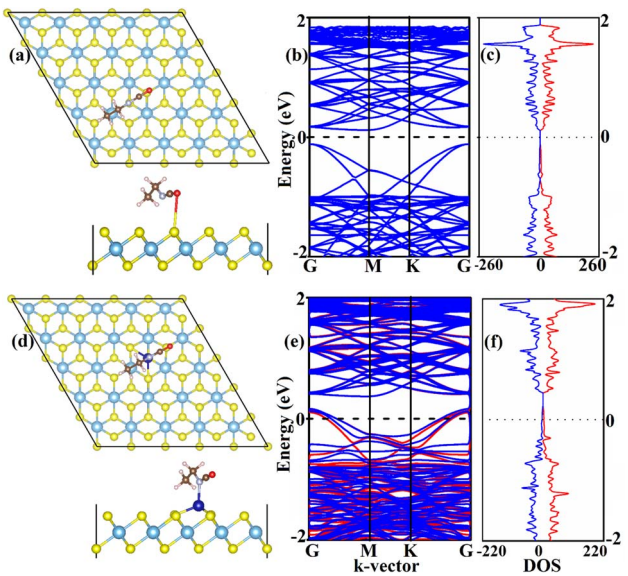

Fig. 4 (a and d) Optimized structures, (b and e) band structures, and (c and f) TDOS of ethylisocyanate (EIC) adsorbed on p-TiS_2 and Co–TiS_2 surfaces, respectively.

adsorption height (h) between the MIC molecule and the TiS_2 surface is 2.98 Å, whereas for the EIC molecule, it is 2.88 Å. These values of h are greater than the sum of the covalent radii (SCR) of the S atom in the TiS_2 surface and the N atom in the adsorbates (1.76 Å). Coupled with the relatively low adsorption energies, these larger h values clearly indicate that the interaction of the adsorbates with the pristine TiS_2 monolayer is characterized by physisorption. Therefore, no chemical bond is formed between the S atoms of p-TiS_2 and the adsorbate atoms.

Decorating the TiS_2 monolayer with Co atoms can enhance its sensitivity toward adsorbates. Different initial configurations of MIC and EIC on Co–TiS_2 (Co–TiS_2@MIC and Co–TiS_2@EIC) are presented in Fig. S7 and S9 in the supplementary information. The optimized adsorption configurations of MIC and EIC on Co–TiS_2 in their most stable orientations are presented in Fig. 3(d) and 4(d) respectively. E_{ads} corresponding to each configuration were calculated and presented in Table 2. E_{ads} analysis indicates that MIC and EIC preferentially anchor to Co–TiS_2 through the N site, resulting in the formation of a Co–N bond, with E_{ads} of −0.81 eV and −0.95 eV, respectively. M. Rouhani studied the adsorption of MIC on B(OH)-doped graphene and calculated the adsorption energy to be −18.15 kcal mol^{-1}, which corresponds to −0.79 eV.[58] To date, no prior reports are available in the literature regarding the adsorption energy of EIC for comparison. The optimal adsorption height corresponding to the maximum adsorption energy is found to be 2.06 Å for both the investigated molecules on Co–TiS_2. The calculated adsorption distances between the surface and MIC(EIC) molecules are 2.06 Å (2.07 Å), respectively. Before adsorption, the average N–C bond length in the MIC and EIC molecules is 1.31 Å and 1.32 Å, which increases to 1.35 Å and 1.36 Å upon adsorption on the Co–TiS_2 surface. The change in bond length indicates the interaction between the VOC molecules and the Co–TiS_2 monolayer.[59]

To gain a deeper insight into the interaction mechanism between VOCs molecules and the adsorbent, a comprehensive analysis of the electronic properties was carried out. The spin-polarized electronic band structure and TDOS spectra of Co–TiS_2@MIC and Co–TiS_2@EIC systems are presented in Fig. 3(e and f) and Fig. 4(e and f), respectively. These spectra reveal that the Co–TiS_2 monolayer system retains its metallic phase upon adsorption. The observed asymmetries in the TDOS spectra of the Co–TiS_2@MIC and Co–TiS_2@EIC systems indicate that the systems maintain their magnetic character after adsorption; however, the magnetic moments of the adsorbed systems are reduced compared to those of the unadsorbed configuration. The spin-polarized PDOS and ODOS spectra of the Co–TiS_2@-MIC system are presented in Fig. 5. From Fig. 5(a), a slight increase in electron density near the Fermi level suggests higher conductivity in the system. The variations in the intensity of the TDOS spectrum across the energy range suggest that adsorption has a significant influence on the distribution of electrons within the Co–TiS_2 system.[60] The appearance of new electronic states and the suppression of some existing ones near the Fermi level upon adsorption reveal significant orbital hybridization between the adsorbent surface and the interacting molecules.[61] The ODOS spectrum of Co-atom and N-atom indicates that the

Table 2 Adsorption energy (E_{ads}) in eV for different orientations of adsorbates (VOCs molecules), vertical distance (h) between molecule and surface in Å, distance (d) between molecule and surface in Å, and total magnetic moment (M) per supercell in μ_B

System	Adsorbed molecule	Orientation of adsorbed molecule	E_{ads}	h	d	M
p-TiS_2	MIC	h_1	−0.14	3.14	3.21	—
		h_2	−0.10	2.98	3.17	—
		h_3	**−0.15**	3.42	3.51	—
		h_4	−0.13	2.79	2.86	—
		v_1	−0.01	2.65	2.73	—
		v_2	−0.03	2.91	3.23	—
Co–TiS_2	MIC	**h_1**	**−0.81**	2.06	2.06	−1.0036
		h_2	−0.73	2.10	2.85	1.0141
		h_3	−0.75	2.08	2.11	1.0135
		h_4	−0.51	2.14	2.28	1.0181
		v_1	−0.10	1.98	1.98	−1.0002
		v_2	−0.60	2.00	2.10	2.5445
p-TiS_2	EIC	h_1	−0.15	3.10	3.22	—
		h_2	−0.16	3.02	3.18	—
		h_3	**−0.17**	3.29	3.35	—
		h_4	−0.16	2.58	2.97	—
		v_1	−0.02	2.49	2.65	—
		v_2	−0.03	2.83	3.27	—
Co–TiS_2	EIC	**h_1**	**−0.95**	2.06	2.07	−2.5542
		h_2	−0.48	2.37	2.46	−1.0105
		h_3	−0.89	1.99	2.08	−2.5341
		h_4	−0.27	2.01	2.01	1.0051
		v_1	−0.59	1.92	1.96	2.6054
		v_2	−0.17	2.06	2.10	−1.0010

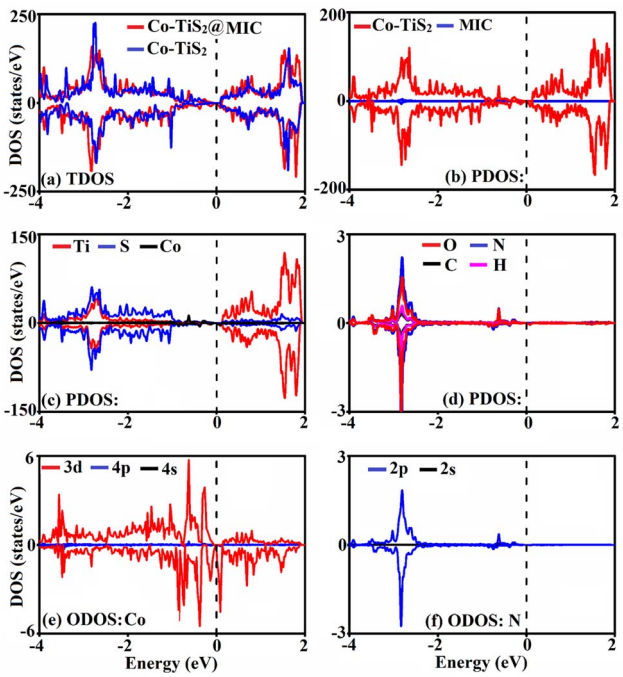

Fig. 5 Total density of states TDOS, partial density of states PDOS and orbital density of states ODOS plots for MIC with Co–TiS_2; (a) TDOS, (b) PDOS, (c) PDOS for adsorbent, (d) PDOS for molecule, (e) ODOS for Co, (f) ODOS for N.

d-orbital of Co-atom overlaps with the p orbital of N-atom at an energy of −0.62 eV near the Fermi level, resulting in a p-d hybridization between N and Co-atom. The TDOS spectrum presented in Fig. 6 shows that the adsorption of the EIC molecule on the Co–TiS_2 surface leads to the emergence of new electronic states in the vicinity of the Fermi level. From Fig. 6(e and f), the ODOS spectrum of Co-atom and N-atom indicates

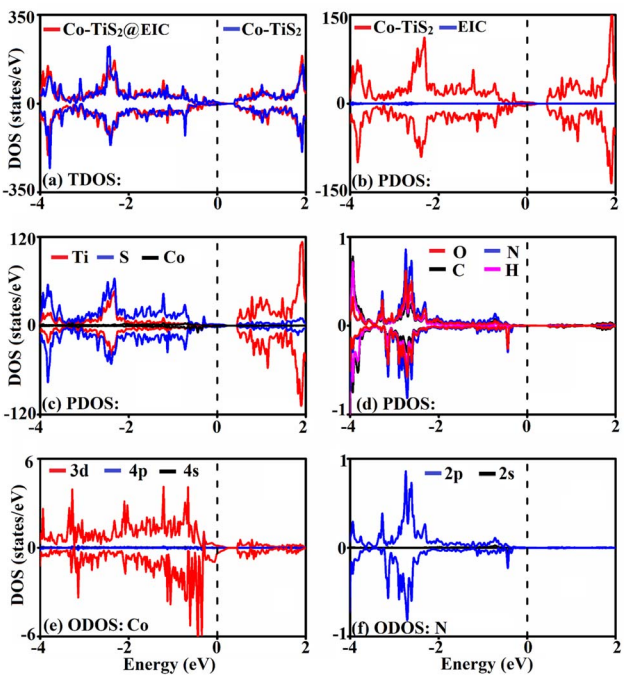

Fig. 6 Density of states DOS for Co–TiS_2 with EIC complex; (a) TDOS, (b) PDOS, (c) PDOS for adsorbent, (d) PDOS for molecule, (e) ODOS for Co, (f) ODOS for N.

that the d-orbital of Co-atom overlaps with the p orbital of N-atom at an energy of −0.43 eV near the Fermi level, resulting in a p-d hybridization between N and Co-atom. This hybridization causes the transfer of charge between the surface and molecule, which causes the bonding between the Co and Ti atoms.

To analyze the charge transfer between the Co–TiS_2 and the adsorbed VOC molecules quantitatively, Bader charge analysis was performed. This analysis helps to identify the donor and acceptor nature of the adsorbate and adsorbent. Herein, we have calculated the partial charge (ΔQ) on each atom of the Co–TiS_2@MIC and Co–TiS_2@EIC systems, which are presented in Fig. 7(a) and (b). The horizontal dotted line acts as a reference line, indicating no charge exchange. Each atom of the system is represented with a distinct color. The positive values of ΔQ indicate the charge donor character, while its negative values show charge acceptor property. From Fig. 7 (a and b), all Ti atoms possess partial positive charges, and all S atoms carry partial negative charges. In both cases, the Co atom of the substrate has a partial positive charge, and the N atom of the adsorbate has a partial negative charge. For the Co–TiS_2@MIC system, the ΔQ on the Co atom of the surface is +0.49e, while the N and O atoms of the molecule carry charges of −1.22e and −1.04e, respectively. In the case of the Co–TiS_2@EIC system, the Co atom has a charge of +0.71e, and the N and O atoms of the molecule have charges of −1.25e and −1.02e, respectively. Thus, for both cases, charges are transferred from the surface to the molecule, indicating that the surface acts as a charge donor while the molecules serve as charge acceptors. The charge acceptance of MIC and EIC might be attributed to their electrophilic nature. The sensing mechanism relies on the process of charge transfer, where a material acts as either a donor or an acceptor. This transfer of charge modifies carrier concentration or resistivity, which is converted into an electrochemical or electrical signal. Thus, the magnitude and direction of charge transfer are critical parameters for assessing sensor efficiency.[62]

Furthermore, the transfer of charge between the surface and molecules alters the work function (ϕ) of the adsorbent. To examine the variations in ϕ, we have calculated the planar-average electrostatic potential (V) of p-TiS_2, Co–TiS_2, Co–TiS_2@MIC, and Co–TiS_2@EIC systems, and presented them in Fig. 8(a and b). The flat region represents the vacuum level E_{vac}, and the negative minima in the potential curve originate from the ionic cores and the crystal potential. The adsorption of MIC and EIC on Co–TiS_2 monolayer systems alters the vacuum level relative to the unadsorbed system. The upward shift in the vacuum level reveals the withdrawal of electrons from the adsorbent, increasing ϕ.[63] Upon the adsorption of MIC(EIC) on the Co–TiS_2 monolayer system, the increase in work function from 5.68 eV to 6.3(6.13) eV was observed. The change in ϕ corresponds to a change in surface dipole moment induced by the adsorption of the VOCs molecules.[64] The variations in the ϕ are correlated with sensitivity (S) values, as expressed by equation.[65]

$$S = \frac{\phi_f - \phi_i}{\phi_i}$$

Where ϕ_i and ϕ_f are the work functions of the Co–TiS_2 system before and after adsorption, respectively. The sensitivity values for MIC and EIC are 10.9 and 7.8%, respectively.

To have a better understanding of the charge transfer between the surface and molecules, the charge density difference (CDD) plots of MIC and EIC molecules on the Co–TiS_2 monolayer system are presented in Fig. 9. The transfer of charge causes a redistribution of electron density, inducing depleted and accumulated charge regions that are distinguished by different colors. In Fig. 9, the yellow and cyan regions correspond to charge depletion and accumulation, respectively. The accumulation of charges occurs around the N atom of adsorbates. In contrast, depletion of charges is observed around the Co atom of Co–TiS_2 systems, indicating charge transfer from the Co atom to the N atom. This is attributed to the higher electronegativity of N compared to Co. The significant charge transfer between the N and Co atoms indicates strong adsorption of the VOC molecules on the Co–TiS_2 surface.

To analyze the nature of chemical bonding between the Co–TiS_2 surface and VOC molecules, specifically whether it is

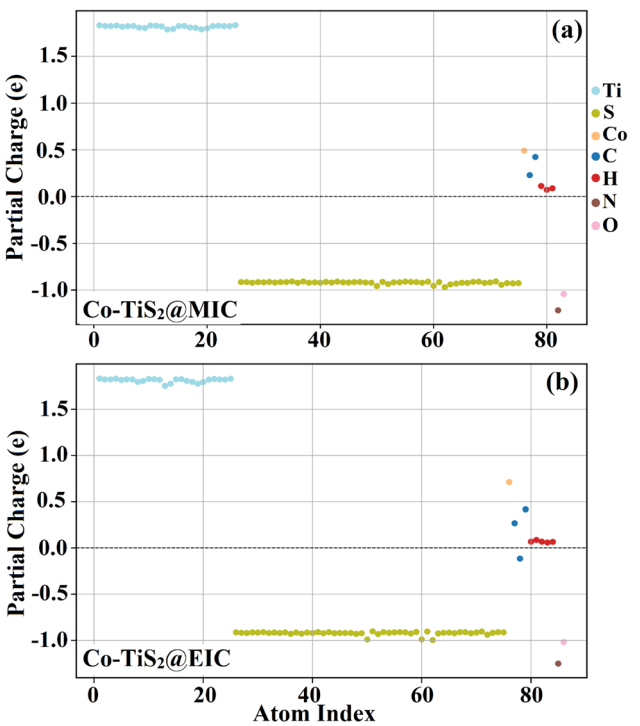

Fig. 7 Partial charge for (a) Co–TiS_2@MIC, (b) Co–TiS_2@EIC.

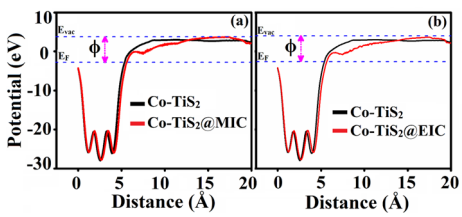

Fig. 8 Electrostatic potential as a function of distance of (a) Co–TiS_2, Co–TiS_2@MIC, (b) Co–TiS_2, Co–TiS_2@EIC.

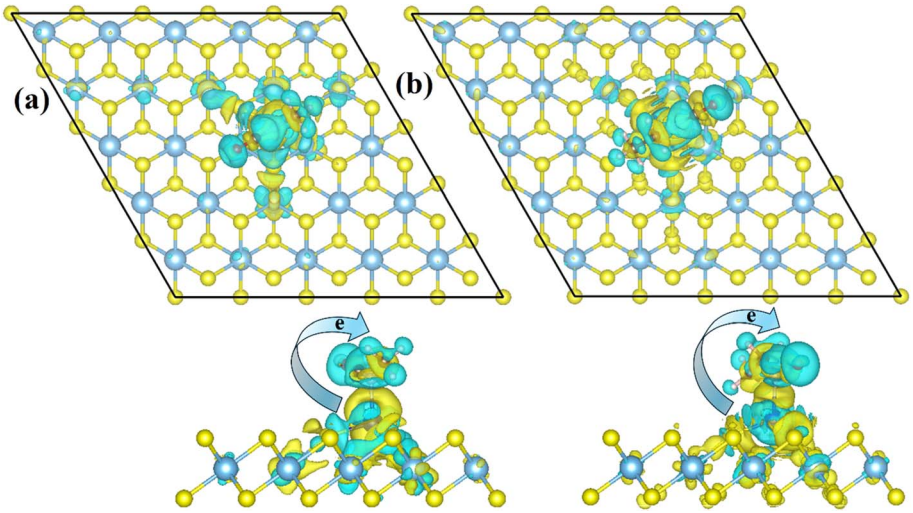

Fig. 9 Charge density difference (CDD) for (a) methylisocyanate (MIC), (b) ethylisocyanate (EIC) adsorbed on Co–TiS_2 monolayer. The isosurface scale is 10^{-3} e Å^{-3}. Yellow and cyan regions indicate charge accumulation and depletion, respectively.

covalent, metallic, or ionic, an electron localization function (ELF) analysis has been performed. Its values range from 0 to 1, where 0 represents completely delocalized and 1 denotes fully localized electrons. In ELF maps, red regions indicate strong electron localization with values close to 1, associated with covalent bonds or lone pairs, and blue regions correspond to values near 0 and represent delocalized electrons. In contrast, green regions with values around 0.5 denote intermediate localization, typically related to ionic or metallic bonding.[66,67] The ELF plots of Co–TiS_2@MIC and Co–TiS_2@EIC systems are shown in Fig. 10. The discrete red and yellow regions between the adsorbate and the surface atoms indicate electron localization and suggest that there is partial electron sharing between the Co atom and the adsorbed VOC molecules. The presence of green and cyan regions further implies moderate electron delocalization associated with charge redistribution at the interface. In contrast, the blue regions represent areas of low electron density, from where the electrons are transferred. Hence, the Bader charge analysis, CDD, and ELF analysis indicate the mixed ionic-covalent interactions.

The recovery time (τ) of a sensor is a critical parameter that defines how long the sensor takes to desorb the adsorbed gas molecules, allowing it to return to its initial state and be ready for the next detection. The shorter recovery time is considered ideal for the reusability of the sensors. The equation gives the recovery time of a sensor is

$$\tau = \alpha^{-1}\exp\left(\frac{|E_{ads}|}{K_\beta T}\right)$$

where α is attempt frequency (1×10^{12} s^{-1}), K_β is the Boltzmann constant and T is the temperature at which the sensor is set to operate, and E_{ads} is the adsorption energy of the system. The calculated recovery times (τ) for MIC and EIC adsorption on the Co–TiS_2 surface are 33 s and 2.6 h at 300 K, respectively, which decrease significantly to 0.46 s and 52 s at 350 K, and further reduce to 15 μs and 1 s at 400 K, indicating faster desorption at

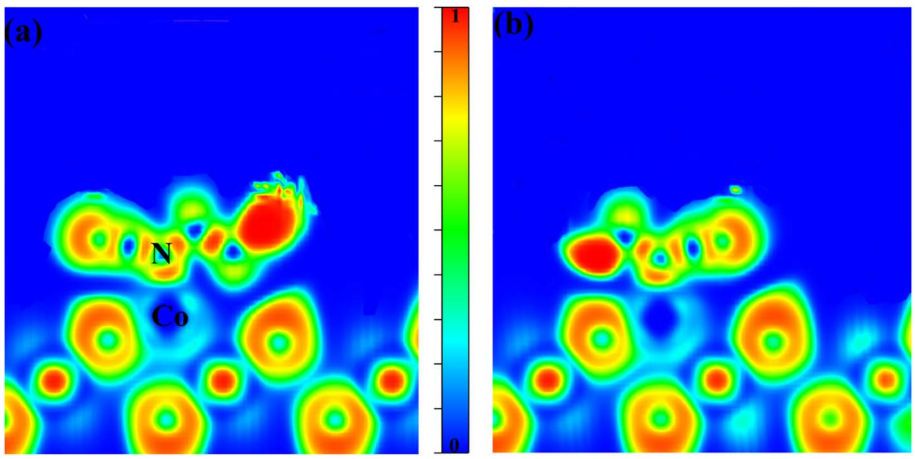

Fig. 10 The electron localization function (ELF) for (a) methylisocyanate (MIC), (b) ethylisocyanate (EIC) adsorbed on Co–TiS_2 monolayer.

elevated temperatures. The efficient and reversible gas sensors exhibit recovery times ranging from milliseconds to a few seconds. In this context, Co–TiS_2-based nanosensors for the detection of MIC and EIC molecules demonstrate recovery times within the desirable range under high-temperature conditions.

4.1 Chemical interactions and COHP analysis

As discussed above, Bader charge analysis and CDD provide a quantitative analysis of the charge exchange between any two elements or reactants. To deeply examine how the two atoms interact, the crystal orbital Hamiltonian population (COHP) provides valuable information. Using COHP, the nature of chemical interaction and its strength can easily be understood. Thus, COHP has a great power to understand the chemistry of the materials. Here, we performed COHP calculations to understand the bonding among various elements, including Ti and S (Ti–S pair), Co and S (Co–S pair), and Co and N (Co–N) pair. Note that the Co–N pair involves the interaction between the adsorbent and the molecule. To easily understand this analysis, we first explain some fundamental concepts. In integrated COHP (ICOHP), the more negative value shows stronger interaction or bonding. In projected COHP (–pCOHP), the bonding states strengthen the interaction that appears in the positive interval (0, N), whereas antibonding states tend to weaken the bonding and appear in the negative interval (–N, 0). The ICOBI value acts as a descriptor for the nature of bonding, covalent, ionic, or mixed. An ICOBI value close to 1 indicates covalent bonding. An intermediate value has an ionic nature. In Fig. 11, the ICOHP value is shown for various orbital interactions. In the Ti–S bond, the strongest interaction is between Ti(4s) and S(2s) orbitals. The other s-d and p-d orbitals have a small or negligible contribution. It means the Ti–S bonding is caused by the overlapping of the 4s orbitals of the Ti atom and the 2s orbitals of the S atoms. For the Co–S bond, the dominant contribution is from the $4p_x$ orbital of the Co atom and the 2s orbital of the S atom. Likewise, in the Co–N pair, the $4p_z$ orbital of Co and the 2s orbital have a strong interaction. Using the concepts, one can understand the interactions for other cases. Fig. 12 provides a more detailed explanation of the results. In Ti–S bonding pairs, maximum energy states below the Fermi level are bonding; however, some antibonding states appear near the Fermi level. A negligible separation between bonding and antibonding states at the Fermi level indicates weak

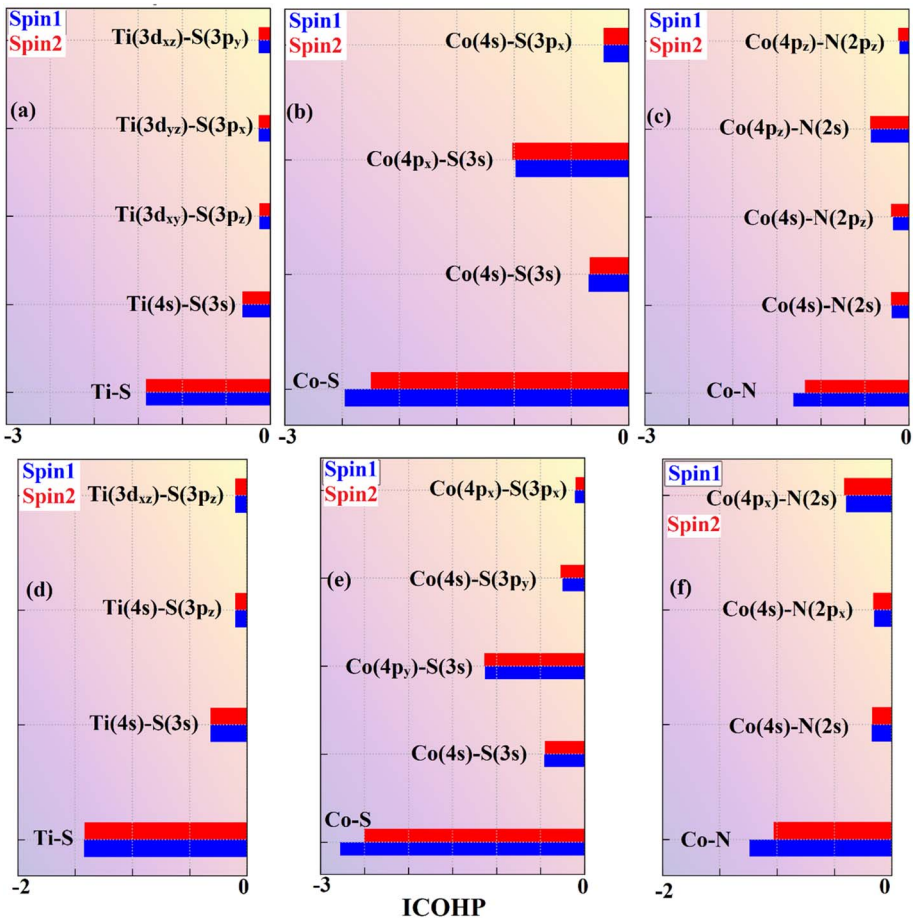

Fig. 11 Integrated crystal orbital Hamiltonian population (ICOHP) analysis; (a) Ti–S bonding pair in Co–TiS_2 with A molecule, (b) Co–S bonding pair in Co–TiS_2 with A molecule, (c) Co–N pair in Co–TiS_2 with A molecule, (d) Ti–S bonding pair in Co–TiS_2 with B molecule, (e) Co–S bonding pair in Co–TiS_2 with B molecule, (f) Co–N pair in Co–TiS_2 with B molecule. A stands for ethylisocyanate, and B is for methylisocyanate. ICOHP values in the majority (minority) spin are shown in blue (red).

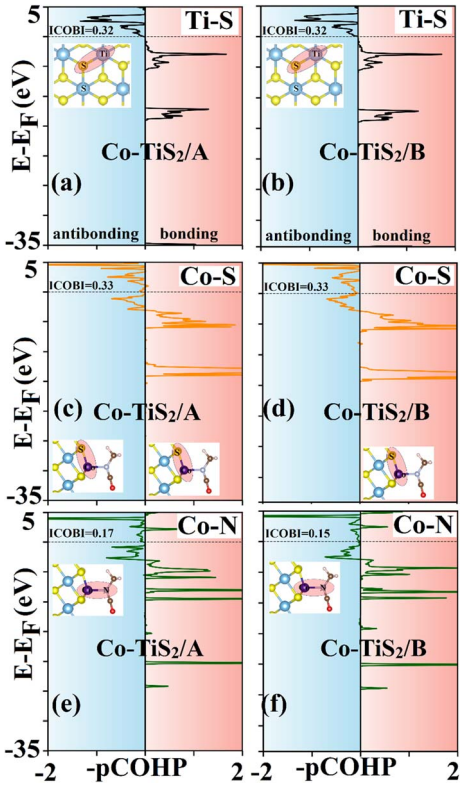

Fig. 12 Projected crystal orbital Hamiltonian population (-pCOHP) analysis; (a) Ti–S bonding pair in Co–TiS_2 with A molecule, (b) Ti–S bonding pair in Co–TiS_2 with B molecule, (c) Co–S bonding pair in Co–TiS_2 with A molecule, (d) Co–S bonding pair in Co–TiS_2 with B molecule, (e) Co–N pair in Co–TiS_2 with A molecule, (f) Co–N pair in Co–TiS_2 with B molecule. Molecules A and B are defined in Fig. 10.

bonding, and it is also reflected by the small value of ICOBI. In Co–S pairs, the bonding states dominate over antibonding ones below −5 eV. The emerging antibonding states above this energy cause a weak interaction, which results in a small ICOBI value. Interestingly, the distribution of bonding/antibonding states in the Co–N pair is similar to that of Co–S. The only difference is in the ICOBI values. The smaller ICOBI value for the Co–N pair shows that Co–N bonding is relatively weaker than the Co–S bonding. To further understand the origin of Co–N interaction, the –pCOHP is plotted for various combinations of Co and N orbitals, shown in Fig. 13. Clearly, the Co(4s) and N(2s) orbitals have a dominant contribution in the bonding states below the Fermi level. The larger peak at −20 eV has a strong influence on the bonding states. In all other orbital interactions, the contribution of bonding states is small. All this discussion reveals that both molecules interact with the adsorbent Co–TiS_2 through the overlapping of Co(4s) and N(2s) bonding orbitals. The slight separation between bonding/antibonding states at the Fermi level and the smaller value of ICOBI confirm that bonding between Co and N is weak ionic bonding. Similarly, the Ti–S and Co–S bonding also has ionic character. Based on p-d hybridization and on the ICOBI values, we proposed that there is mixed covalent-ionic bonding between the Co-atom of the adsorbent and the N-atom of the VOC molecules.

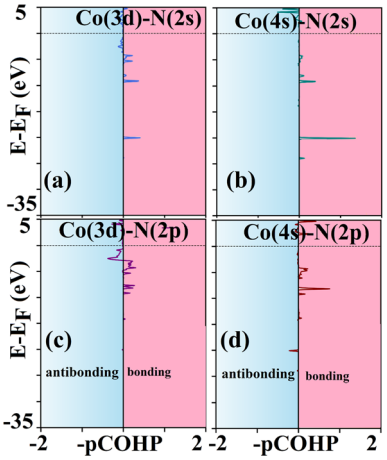

Fig. 13 Projected COHP (−pCOHP) for (a) Co(3d) and N(2s) orbitals, (b) Co(4s) and N(2s), (c) Co(3d) and N(2p) orbitals, (d) Co(4s) and N(2p) orbitals.

5 Conclusion

DFT calculations were performed to explore the geometrical, electronic, and magnetic properties of pure and Co-decorated TiS_2 monolayer systems. The nature and strength of chemical bonding was examined using COHP analysis. The adsorption of two selected volatile organic compounds (VOCs), methylisocyanate (MIC) and ethylisocyanate (EIC), was also investigated on these monolayer systems. Our results showed that pristine TiS_2 systems exhibited poor adsorption towards the targeted VOC molecules. The anchoring of Co-atom on the TiS_2 surface induces a phase transformation from the semiconducting to metallic, remarkably improving its interaction with VOCs molecules. The obtained adsorption energies for MIC and EIC on the Co–TiS_2 monolayer systems are −0.81 eV and −0.95 eV, respectively. The results indicated that both MIC and EIC acted as charge acceptors, whereas Co–TiS_2 acted as an electron donor. Furthermore, the density of states, Bader charge, electrostatic potential, work function, and electron localization function analysis were performed to authenticate the adsorption of targeted VOCs on the Co–TiS_2 surface. COHP results showed that the Co atom forms ionic weak ionic bonding with the N atom of the molecule by Co(4s) and N(2s) orbitals. Although the sensitivity and selectivity of Co–TiS_2-based nanosensors are good towards MIC and EIC molecules, they demonstrate poor recovery times at room temperature, which can hinder their reusability at room temperature, the desired recovery times can be achieved at elevated temperatures. Based on our results, we propose that the Co–TiS_2 monolayer could be used as a sensor for the detection of MIC and EIC molecules efficiently.

Conflicts of interest

The authors have no conflicts of interest to declare.

Data availability

Data sets generated during the current study are available from the corresponding author (Dr M. Mushtaq) upon reasonable request.

Supplementary information (SI) is available. See DOI: https://doi.org/10.1039/d5ra09215a.

Acknowledgements

Dr M. Mushtaq acknowledges the support of the University of Poonch Rawalakot for the VASP code license.

References

1 E. David and V.-C. Niculescu, *Int. J. Environ. Res. Publ. Health*, 2021, **18**, 13147.
2 Y. Ren, X. Guan, Y. Peng, A. Gong, H. Xie, S. Chen, Q. Zhang, X. Zhang, W. Wang and Q. Wang, *J. Environ. Manage.*, 2024, **357**, 120730.
3 A. Mangotra and S. K. Singh, *J. Biotechnol.*, 2024, **382**, 51–69.
4 X. Lian, J. Guo, Y. Wang, S. Wang and J. J. T. Li, *Toxics*, 2024, **12**, 438.
5 C.-J. Chang, H.-H. Yang, C.-A. Chang and H.-Y. Tsai, *Aerosol Air Qual. Res.*, 2013, **13**, 237–242.
6 Z. Wang, X. Zhang, L. Wang, S. Fu, J. Wu, J. Xiong and S. Huang, *Atmos. Environ.*, 2024, **339**, 120855.
7 S. Dutta, P. Sengupta, S. Bagchi, B. S. Chhikara, A. Pavlík, P. Sláma and S. Roychoudhury, *Front. Cell Dev. Biol.*, 2023, **11**, 1162015.
8 N. Ding, S. Batterman and S. K. Park, *J. Wom. Health*, 2020, **29**, 65–73.
9 C. H. Halios, C. Landeg-Cox, S. D. Lowther, A. Middleton, T. Marczylo and S. Dimitroulopoulou, *Sci. Total Environ.*, 2022, **839**, 156201.
10 C. S. Senthilkumar, N. K. Sah and N. Ganesh, *Asian Pac. J. Cancer Prev. APJCP*, 2012, **13**, 2429–2435.
11 F. M. De Souza, P. K. Kahol and R. K. Gupta, in *Polyurethane Chemistry: Renewable Polyols and Isocyanates*, ACS Publications, 2021, pp. 1–24.
12 B. D. Etz, C. M. Woodley and M. K. Shukla, *J. Hazard. Mater.*, 2024, **473**, 134628.
13 E. Broughton, *Environ. Health*, 2005, **4**, 6.
14 B. B. Ganguly and S. Mandal, *Mutat. Res., Genet. Toxicol. Environ. Mutagen.*, 2017, **824**, 9–19.
15 P. G. Harrison and E. W. Thornton, *Faraday Trans. 1 Phys. Chem. Condens. Phases*, 1976, **72**, 1317–1323.
16 M. Pawlak, K. Pobłocki, J. Drzeżdżon, B. Gawdzik and D. Jacewicz, *Sci. Total Environ.*, 2024, **934**, 173250.
17 O. Geiss, G. Giannopoulos, S. Tirendi, J. Barrero-Moreno, B. R. Larsen and D. Kotzias, *Atmos. Environ.*, 2011, **45**, 3676–3684.
18 S. Singh, S. S, P. Varma, G. Sreelekha, C. Adak, R. P. Shukla and V. B. Kamble, *Microchim. Acta*, 2024, **191**, 196.
19 S. Yang, C. Jiang and S.-h. J. Wei, *Appl. Phys. Rev.*, 2017, **4**, 21304.
20 S. S. Varghese, S. H. Varghese, S. Swaminathan, K. K. Singh and V. J. E. Mittal, *Electronics*, 2015, **4**, 651–687.
21 J. Wang, W. Zeng and Q. Zhou, *Front. Chem.*, 2022, **10**, 950974.
22 C. Fang, R. De Groot and C. Haas, *Phys. Rev. B:Condens. Matter Mater. Phys.*, 1997, **56**, 4455.
23 J. Zhang, X. Qin, H. Xin, D. Li and C. J. Song, *J. Electron. Mater.*, 2011, **40**, 980–986.
24 C. Xu, P. A. Brown and K. L. Shuford, *RSC Adv.*, 2015, **5**, 83876–83879.
25 S. B. Basuvalingam, Y. Zhang, M. A. Bloodgood, R. H. Godiksen, A. G. Curto, J. P. Hofmann, M. A. Verheijen, W. M. Kessels and A. A. Bol, *Chem. Mater.*, 2019, **31**, 9354–9362.
26 N. Sakhuja, R. K. Jha, R. Chaurasiya, A. Dixit and N. Bhat, *ACS Appl. Nano Mater.*, 2020, **3**, 3382–3394.
27 K. Y. Shin, Y. Kim, A. Mirzaei, H. W. Kim and S. S. J. C. Kim, *J. Mater. Chem. C*, 2025, **13**, 10434–10436.
28 S. M. Majhi, A. Mirzaei, S. Navale, H. W. Kim and S. S. J. N. Kim, *Nanoscale*, 2021, **13**, 4728–4757.
29 K. Y. Shin, Y. Kim, A. Mirzaei, H. W. Kim and S. S. Kim, *J. Mater. Chem. C*, 2025, **13**, 10434–10436.
30 A. Mirzaei, H. R. Ansari, M. Shahbaz, J.-Y. Kim, H. W. Kim and S. S. J. C. Kim, *Chemosensors*, 2022, **10**, 289.
31 G. Liu, Y. Wang, J. Li, Y. Liu and M. Salehabadi, *J. Sulfur Chem.*, 2021, **42**, 40–50.
32 H. Liu, Z. Tan, Y. Niu, S. Wang and Y. Wang, *Chem. Phys. Lett.*, 2023, **818**, 140410.
33 H. Wu, W. Zhang, H. Yuan, G. Lin, H. Xie and T. Jiang, *J. Alloys Compd.*, 2025, **1010**, 178139.
34 J. Shi, W. Quan, X. Chen, X. Chen, Y. Zhang, W. Lv, J. Yang, M. Zeng, H. Wei and N. Hu, *Phys. Chem. Chem. Phys.*, 2021, **23**, 18359–18368.
35 F. M. Altalbawy, F. F. Sead, S. V. Mayani, A. Kumar, G. PadmaPriya, A. Kashyap, V. KAVITHA, K. K. Joshi, D. Abduvalieva and K. J. M. C. Muzammil, *Phys., Mater. Chem. Phys.*, 2025, 131385.
36 S. A. Toularoud, H. Hadipour and H. R. Soleimani, *Phys. B*, 2024, **694**, 416413.
37 F. Ghani, A. A. Haidry, A. Raza, Q. Fatima, Y. Weng, M. Sajjad, M. D. Albaqami and S. Mohammad, *Mater. Today Commun.*, 2024, **40**, 109680.
38 T. Tang, Z. Li, Y. Y. Liu, Y. L. Chen, Y. F. Cheng, Y. Liang, J. H. Zhuang, X. Y. Hu, A. Jannat, R. Ou and K. Xu, *Ceram. Int.*, 2025, **51**, 3216–3223.
39 S. Zhang, L. Tao, H. Zhang, H. Zhao, F. Di, L. Li and B. J. S. An, *Interfaces*, 2025, 107553.
40 G. Kresse and J. Furthmüller, *Phys. Rev. B:Condens. Matter Mater. Phys.*, 1996, **54**, 11169.
41 P. E. Blöchl, *Phys. Rev. B:Condens. Matter Mater. Phys.*, 1994, **50**, 17953.
42 J. P. Perdew, K. Burke and M. Ernzerhof, *Phys. Rev. Lett.*, 1996, **77**, 3865.
43 S. Grimme, J. Antony, S. Ehrlich and H. Krieg, *J. Chem. Phys.*, 2010, **132**, 154104.
44 C. Y. Lin, L. Zhang, Z. Zhao and Z. Xia, *Adv. Mater.*, 2017, **29**, 1606635.
45 I. Muhammad, M. Mushtaq, Z. Leilei, M. A. R. Khan, K. Qasim, M. Sabir, S. A. Abdelmohsen, M. M. Alanazi, A. Laref and N. J. R. A. Hadia, *RSC Adv.*, 2025, **15**, 8938–8947.
46 B. Chakraborty, A. Vaidyanathan, G. Sanyal, S. Lakshmy and N. Kalarikkal, *J. Appl. Phys.*, 2022, **132**, 084502.

47 L. Lin, L. Han, K. Xie, C. Hu and Z. Dong, *FlatChem*, 2022, **36**, 100421.
48 M. Inoue, H. P. Hughes and A. D. Yoffe, *Adv. Phys.*, 1989, **38**, 565–604.
49 B. Xu, Y.-S. Wang, N.-H. Song, J. Zhang, M. Li and L. Yi, *Chin. Phys. Lett.*, 2016, **33**, 016802.
50 S. A. Toularoud, H. Hadipour and H. R. Soleimani, *Phys. B*, 2024, **694**, 416413.
51 A. H. Reshak and S. Auluck, *Phys. Rev. B: Condens. Matter Mater. Phys.*, 2003, **68**, 245113.
52 H. Liu, S. Yang, G. Lei, M. Xu, H. Xu, Z. Lan, Z. Wang, J. Xiong and H. Gu, *Int. J. Hydrogen Energy*, 2022, **47**, 12096–12106.
53 H. Liu, S. Yang, G. Lei, M. Xu, H. Xu, Z. Lan, Z. Wang, J. Xiong and H. Gu, *Int. J. Hydrogen Energy*, 2022, **47**, 12096–12106.
54 A. H. Reshak and S. Auluck, *Phys. Rev. B:Condens. Matter Mater. Phys.*, 2003, **68**, 245113.
55 U. Iqrar, S. S. Alarfaji, G. Nabi and M. I. Khan, *Int. J. Hydrogen Energy*, 2025, **169**, 151115.
56 M. I. Khan, M. I. Akber, M. Gul, T. Iqbal, S. S. Alarfaji and A. J. R. A. Mahmood, *RSC Adv.*, 2024, **14**, 7040–7051.
57 V. Shukla, *Mater. Adv.*, 2020, **1**, 3104–3121.
58 M. Rouhani, *Inorg. Chem. Commun.*, 2021, **127**, 108552.
59 T. Li, Q. Miao, Y. Wang, H. J. S. Yang and Interfaces, *Surf. Interfaces*, 2023, **42**, 103336.
60 S. Tan, M. Bi, S. Lei, X. He, X. Hu, J. He and T. Jiang, *Comput. Theor. Chem.*, 2024, **1236**, 114586.
61 F. Opoku and P. P. Govender, *Appl. Surf. Sci.*, 2020, **525**, 146590.
62 R. N. Ahmed, M. A. Rauf Khan, S. Akhtar, A. Ahmed, T. Hussain and M. Mushtaq, *Prog. Nat. Sci. Mater. Int.*, 2025, **35**, 905–916.
63 N. Viveka, C. Poornimadevi, C. P. Kala, D. J. J. S. Thiruvadigal and Interfaces, *Surf. Interfaces*, 2025, 106579.
64 P. C. Rusu and G. Brocks, *J. Phys. Chem. B*, 2006, **110**, 22628–22634.
65 S. Khammuang, A. Udomkijmongkol, S. Thasitha, T. Hussain and K. Kotmool, *Appl. Surf. Sci.*, 2025, **699**, 163110.
66 T. Alaa Hussein, N. M. Shiltagh, W. Kream Alaarage, R. R. Abbas, R. A. Jawad and A. H. Abo Nasria, *Results Chem.*, 2023, **5**, 100978.
67 H. Levämäki and L. Vitos, *Phys. Rev. B*, 2021, **103**, 035118.